



Research Article

Effect of aliovalent substituted highly disordered GeTe compound's thermoelectric performance



Khasim Saheb Bayikadi^{a,b,1}, Safdar Imam^{a,c,1}, Mohammad Ubaid^d, Anver Aziz^d, Kuei-Hsien Chen^b, Raman Sankar^{a,*}

^a Institute of Physics, Academia Sinica, Taipei 11529, Taiwan

^b Institute of Atomic and Molecular Sciences, Academia Sinica, Taipei 10617, Taiwan

^c Department of Physics, National Taiwan Normal University, Taipei 11677, Taiwan

^d Department of Physics, Jamia Millia Islamia, New Delhi 110025, India

ARTICLE INFO

Article history:

Received 7 February 2022

Received in revised form 4 July 2022

Accepted 5 July 2022

Available online 8 July 2022

Keywords:

Vacancy control

Doping optimization

Atomic disorder

Thermal conductivity

Figure of merit

ABSTRACT

As a lead-free high-performance thermoelectric material, germanium telluride (GeTe) has recently been extensively studied for mid-temperature (500–800 K) applications. The carrier concentration and the thermal conductivity are reduced for vacancy-controlled GeTe compounds compared with pristine GeTe. We explored and optimized the $\text{Ge}_{0.9-x}\text{Sb}_{0.1}\text{P}_x\text{Te}$ ($x = 0.01\text{--}0.05$) material's highest thermoelectric performance at elevated temperatures. Intrinsic Ge vacancy control and manipulation of Ge (+2) with Sb/P (+3) increased the charge contribution to power factor improvement to $\sim 42 \mu\text{Wcm}^{-1} \text{K}^{-2}$ while minimizing the lattice thermal contribution to $\sim 0.4 \text{ W/mK}$. This resulted in an increase in thermoelectric performance of ~ 2.4 @ 773 K for the $\text{Ge}_{0.88}\text{Sb}_{0.1}\text{P}_{0.02}\text{Te}$ sample. The inclusion of atomically disordered Sb/P ions considerably increases the scattering effects caused by the point defect, whereas stretched grain boundaries reveal the decreased lattice thermal contribution. The current work demonstrates the effectiveness of phosphorus as a co-dopant in increasing the average thermoelectric performance (ZT_{avg}) value over the GeTe operating temperature range.

© 2022 Published by Elsevier B.V.

1. Introduction

Among renewable energy technologies, thermoelectric (TE) energy conversion may directly convert waste heat to useable electrical energy or vice versa. Thermoelectric materials may bring the investigation of alternate energy sources to completion, allowing for the resolution of various contemporary energy challenges. Numerous technologies are being researched to reduce waste thermal energy and harness it as a possible energy source [1–4]. The dimensionless quantity (ZT) represents the conversion performance of a TE material, comprehended as the figure of merit:

$$ZT = (S^2\sigma/\kappa) T \quad (1)$$

where S and σ are Seebeck coefficient (thermopower) and electrical conductivity, respectively, κ is the total thermal conductivity, and T is

the absolute temperature of the material. Whereas $\kappa = \kappa_{\text{ele}} + \kappa_{\text{lat}}$ is total thermal conductivity, a combination of κ_{ele} is due to electrons, and κ_{lat} is due to phonons [5]. As the statement indicates, at the specific operating temperature (T), any TE material with high electrical conductivity, a high Seebeck coefficient, and low total thermal conductivity may produce a high ZT . The experimental results, on the other hand, seem to be either way due to the optimization of many factors involved in ZT expression. The most common method for boosting ZT is mainly dependent on two procedures: Firstly, band engineering and optimizing the concentration of carriers (n) may increase the power factor (PF, σS^2); secondly, nano and micro-structure characteristics that facilitate phonon scattering, such as vacancies, secondary phases, mesoscale grain boundaries, and so on can reduce the lattice portion of thermal conductivity (κ_{lat}) [6–15].

GeTe, a well-known TE material since the 1960 s, has recently received a lot of attention owing to its mid-temperature high TE capabilities. Because of its large concentration of Ge vacancies ($\sim 10^{21} \text{ cm}^{-3}$), it has an extremely low Seebeck coefficient ($\sim 34 \mu\text{V/K}$), very high electrical conductivity ($\sim 8500 \text{ S/cm}$), and high thermal conductivity ($\sim 8 \text{ W/m K}$) at room temperature (RT) [16]. As a result, the

* Corresponding author.

E-mail address: sankarraman@gate.sinica.edu.tw (R. Sankar).

¹ Equal contributing authors.

pristine GeTe has a relatively low TE performance. Doping, forming different composites, micro/nanostructure fabrication, and recrystallization improve the TE properties of GeTe [17–19]. However, at around 700 K, GeTe undergoes a phase transition from a rhombohedral (low-temperature r-GeTe) to a cubic structure (c-GeTe, high-temperature). The phase transition caused by the high Ge vacancy causes minor distortion along the [111] direction as well as band (L) splitting [20–22]. Furthermore, it has been noted that the decrease of the phase transition in GeTe can be affected by entropy manipulation using a variety of dopants. Reducing phase transition can improve TE material performance over a wide temperature range and increase long-term thermal strength [12,14,23]. Compared to c-GeTe, r-GeTe has less symmetry and switching between the valance band's L and Σ energy levels is the most unusual feature. This feature gives us an additional dimension to manipulate the band in order to improve electronic properties and achieve high band degeneracy [24]. Thus, at elevated temperatures, c-GeTe exhibits a comparable high power factor to r-GeTe (L and Σ contribute collectively to Seebeck) [25,26].

Improvements in scientific advancement have enabled us to achieve high-performance TE materials. Besides the strategies mentioned earlier, chemical doping has historically been employed to enhance the TE parameters, especially n , while maintaining high carrier mobility (μ) [11,14]. The aliovalent Sb doping is proved to optimize n and κ concurrently to attain high ZT. The Sb substituted GeTe compounds (GST) reduce the intrinsic n by reducing the rhombohedral-cubic phase transition temperature and efficiently minimizing the κ due to more scattering of phonons [27,28]. The aliovalent ions co-doping accompanying some additional TE materials have improved the ZT, such as Sb-Cu [29–31], Sb-Se [32], Sb-Mg [33,34], Sb-Cd [35], Sb-In [36], Sb-Mo [37], Sb-Mn [38,39], Sb-S/Se [40], and Sb-Pb [41]. Recently, Y-doped GeTe was found to increase the interaxial angle due to a decrease in n (donor effect), leading to high TE performance. Moreover, the Bi/Y doped GeTe sample achieved a ZT of ~ 1.8 at 723 K [42]. Another study demonstrated an excellent RT power factor of $2800 \text{ mW m}^{-1}\text{K}^{-2}$, using Cu_2Te alloying, which lowers the n while maintaining μ , and resonant In doping, which enhances the Seebeck in the GeTe-based systems. A high ZT of ~ 2.1 at 723 K and impressive single-leg efficiency of $\sim 11.8\%$ between 323 and 745 K was achieved [43]. Defect engineering on cation sites is also an effective way of optimizing the TE parameters of GeTe-based systems. The Ti co-doping in GeTe increases the effective mass from $\sim 1.13 m_0$ to $\sim 1.71 m_0$, and further doping of Bi reduces the n from $\sim 8.21 \times 10^{20} \text{ cm}^{-3}$ (pristine GeTe) to $\sim 3.25 \times 10^{20} \text{ cm}^{-3}$, resulting in a maximum ZT of ~ 1.89 at 735 K in $\text{Ge}_{0.945}\text{Ti}_{0.015}\text{Bi}_{0.06}\text{Te}$ [44]. In recent work, the effect of rare earth elements doping on the TE properties of GeTe shows promising results with enhanced Seebeck due to the local magnetic moment emerging from the substitution of these elements, resulting in improved PF. This study provides a path to optimizing GeTe-based systems' TE properties with further co-doping of Bi/Sb [45].

Considerable efforts on GeTe-based TE materials have been devoted in the past few years; moreover, consistent achievement of high performances further pushes us to explore this material to the fullest. Previously, we studied the impacts of antimony (Sb) and phosphorus (P) doping and GeP secondary phase effects on the TE properties of the GeTe system [46]. Afterward, optimizing our two-step synthesis process, we enhanced the ZT value of the GeTe system from 0.8 to 1.37 at 773 K by controlling the Ge-vacancy and revealing its analogous herringbone-structured micro-domains [22]. Motivated by our previous work on GeTe [22], $\text{Ge}_{0.9}\text{Sb}_{0.1}\text{Te}$ [27], and current knowledge of its related materials, we optimized the $\text{Ge}_{0.9-x}\text{Sb}_{0.1}\text{P}_x\text{Te}$ system's TE performance. We prepared $\text{Ge}_{0.9-x}\text{Sb}_{0.1}\text{P}_x\text{Te}$ (where $x = 0.01, 0.02, 0.03, 0.04, \text{ and } 0.05$) samples and investigated P content's influence on the GeTe system's TE properties. With Sb/P doping on GeTe, the n could be tuned to the

desired value, and valence band convergence was achieved with Sb doping in the GeTe. Aside from that, the mass fluctuation of Ge, Sb, and P significantly improved the scattering effects induced by point defects and strain grain boundaries, as well as the presence of more phonon scattering centers. Finally, $\text{Ge}_{0.88}\text{Sb}_{0.1}\text{P}_{0.02}\text{Te}$ exhibits a noteworthy high ZT value of ~ 2.4 , accompanying the high power factor of $\sim 42 \mu\text{Wcm}^{-1}\text{K}^{-2}$ and low total thermal conductivity of $\sim 1.35 \text{ W/mK}$ at 773 K. Our analysis of Sb/P doped GeTe will pave the way for room and mid-temperature TE applications.

2. Experimental section

2.1. $\text{Ge}_{0.9-x}\text{Sb}_{0.1}\text{P}_x\text{Te}$ sample preparation

We processed and used Germanium (Ge–99.999 %), Antimony (Sb–99.999 %), Phosphorus (P–99.999 %), and Tellurium (Te–99.997 %) metals bought from Sigma Aldrich for the preparation of the samples. After sealing all samples in highly evacuated ($< 50 \text{ mTorr}$) quartz tubes, a series of $\text{Ge}_{0.9-x}\text{Sb}_{0.1}\text{P}_x\text{Te}$ samples (labeled as $x = 0.01(\text{GSPT-1}), 0.02(\text{GSPT-2}), 0.03(\text{GSPT-3}), 0.04(\text{GSPT-4}), \text{ and } 0.05(\text{GSPT-5})$) were melted at 700°C for 24 h to generate initial compositions. The cooled ingots were crushed into a fine powder and enclosed in an empty two-fold quartz tube for 48 h of melt quench in air annealing at 900°C . Our previous work on undoped GeTe revealed the specifics of the two-step melt-quenching technique [22].

2.2. Structural and chemical characterization

The Bruker D8 diffractometer with Cu K_α radiation ($\lambda = 1.5406 \text{ \AA}$) was utilized for X-ray diffraction (XRD) measurements to determine the phase purity of the sample powders. The temperature-dependent XRD was investigated using the Taiwan Photon Source (TPS) at the National Synchrotron Radiation Research Center (NSRRC) in Taiwan. We used Field Emission Scanning Electron Microscopy (FESEM) in conjunction with Energy Dispersive Spectroscopy (EDS) to validate elemental compositions (JEOL JSM-6700 F). High-resolution Transmission Electron Microscopy (HRTEM) investigations were performed on the microstructures utilizing the Tecnai G2 F30 STWIN TEM apparatus with a field emission gun capability of 200 kV.

2.3. Computational studies

Ab-initio density functional theory (DFT) calculations using the Quantum ESPRESSO program were performed to better understand the effect of Sb and P dopants on the electronic states of GeTe [47]. We employed ultra-soft pseudo potentials (USPP) with kinetic energy and charge density cutoffs of 550 eV and 4400 eV, respectively, to describe electron-ion interactions [48]. We have adopted generalized gradient approximation (GGA) with the Perdew-Burke-Ernzerhof (PBE) exchange-correlation functional [49]. The Brillouin zone was sampled using the Monkhorst-Pack grid [50] of $5 \times 5 \times 1$ and $10 \times 10 \times 1$ for relaxation and static calculations, respectively. The lattice vectors and atomic positions were fully relaxed to obtain the optimized configuration through the bfgs method.

2.4. Thermoelectric property measurements

The annealed ingots were crushed into a fine powder, and cylindrical pellets were made in a hot press at 60 MPa pressure at 550°C for 10 min in a high vacuum of 10^{-5} Torr using a graphite die ($\sim 20 \text{ mm}$). We used the standard Archimedes approach to determine the densities (ρ) of the sintered pellets and found that they were close to 97–98 % of the theoretical density. For the thermal diffusivity and electrical transport experiments, all pellets were divided

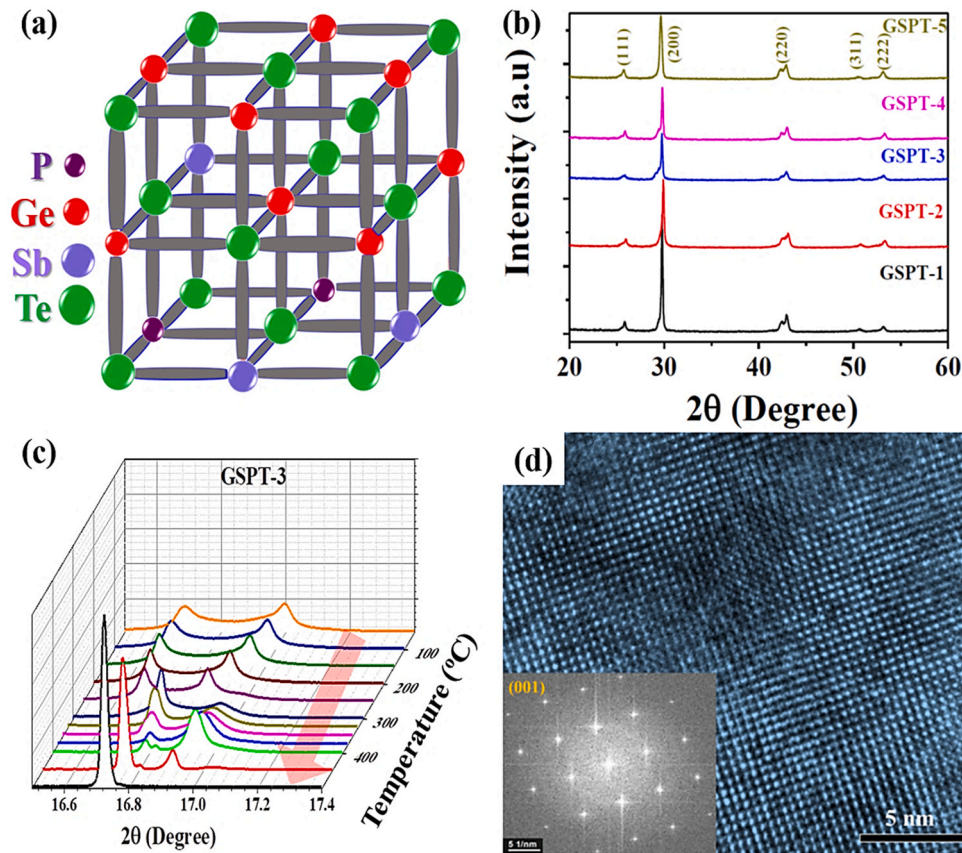


Fig. 1. (a) Schematic GeTe pseudo-cubic structure after Sb/P doping; (b) Powder XRD patterns of P co-doped $\text{Ge}_{0.9}\text{Sb}_{0.1}\text{Te}$; (c) Temperature-dependent XRD patterns of the GSPT-3; and (d) HR-TEM analysis of pseudo-cubic domain nature (inset: SAED pattern).

into square and rectangular pieces. The thermal diffusivity (D) and specific heat (C_p) of square pellets (6×6 mm and thickness ~ 2 mm) were measured using the laser flash technique (LFA 457, NETZSCH) with pyroceram standard calibration using the Dulong–Petit law. Total thermal conductivity and lattice thermal conductivity were calculated using $\kappa = D C_p \rho$ and $\kappa_{lat} = \kappa - \kappa_{ele}$, respectively. Using Wiedemann–Franz law $\kappa_{ele} = L_o \sigma T$, electrical thermal conductivity (κ_{ele}) was calculated, whereas L_o is the Lorenz number calculated by an empirical equation of $1.5 + \exp(-|S|/116)$. Around $\sim 5\%$ uncertainty was estimated for thermal conductivity measurements. The carrier transport characteristics and S were measured simultaneously on a ZEM-3 ULVAC, utilizing a cut and polished pellet of parallelepiped shape ($3 \times 2 \times 15$ mm³) in a He gas atmosphere with a $\sim 5\%$ uncertainty estimate for each parameter. The Hall coefficient was determined using a PPMS AC transport 5-point probe measurement in a magnetic field of up to 5 T. To calculate the carrier concentration (n) and mobility (μ), the equations $n = 1/(eR_h)$ and $\mu = \sigma R_h$ were employed, where e indicates the electron charge, and R_h represents the Hall coefficient. Error bars are not included in all figures for clarity purposes.

3. Results and discussion

3.1. Crystal symmetry and microstructure analysis

In the mid-range temperature, GeTe-based compounds are an encouraging TE material due to their application. The crystal structures of pseudo-cubic GeTe, with Sb/P atoms occupying the Ge site, are shown in Fig. 1(a). The $\text{Ge}_{0.9-x}\text{Sb}_{0.1}\text{P}_x\text{Te}$ sample's synthesized

powder X-ray diffraction (PXRD) patterns are shown in Fig. 1(b). The PXRD results were obtained on the solid-state melt quenching sample powders, confirming that all samples of $\text{Ge}_{0.9-x}\text{Sb}_{0.1}\text{P}_x\text{Te}$ resemble the pseudo-cubic ($R\bar{3}m$ and $Fm\bar{3}m$) phase. The merger of two peaks in the range 40° – 45° gradually up to 3 at% of P content by fixed GST's composition, which can significantly influence the Seebeck coefficient, confirms the rhombohedral to pseudo-cubic transformation at RT [51]. Additionally, the shifting of samples' peaks towards the lower angle side, corresponding to the (200) plane, indicates that P doping into the Ge site leads to strain, implying increasing lattice d -spacing. Due to the enhanced d -spacing, the lattice strain and stacking faults will also create an additional strain that further increases the phonon scattering to lower the κ_{lat} [11,14]. We used synchrotron X-ray diffraction of a GSPT-3 sample at various temperatures to better understand the temperature-dependent phase transition in GeTe, as shown in Fig. 1(c). The temperature-dependent XRD of the composition clearly shows the transition from rhombohedral to simple cubic phase at 350°C (623 K). The synchrotron X-ray diffraction of GSPT-5 is shown in Fig. S1. The cubic phase, which is comparable to cubic GeTe, is visible in the high-temperature XRD pattern [52]. Because of the symmetric cubic structure, all samples demonstrate a phase change from 523 to 623 K, making them more electrically conductive than the previous phase. In this stable phase, the Ge atom's thermal strain-induced variation pushes the unit cell's deformity back along [111] orientation with an angular shift of 1.65° [20]. The electrical conductivity of all $\text{Ge}_{0.9-x}\text{Sb}_{0.1}\text{P}_x\text{Te}$ samples also reflects these structural phase transitions. Fig. 1(d) shows the HR-TEM picture of the GSPT-2, which indicates its pseudo-cubic nature, and the inset shows the Fast

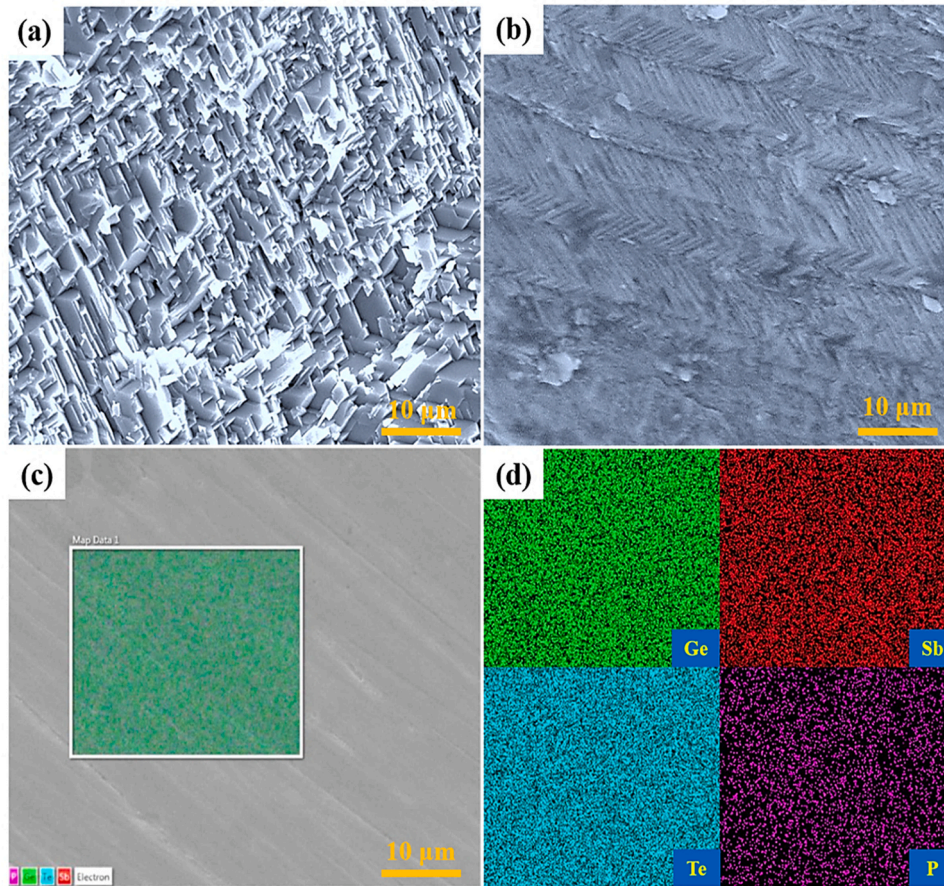


Fig. 2. SEM images of the free fractured surface of the GSPT-2 pellet; (a) High-density fractal structure; (b) Existing herringbone structures; (c and d) SEM image and elemental mapping of the GSPT-2 sample, respectively.

Fourier Transformed (FFT) diffraction pattern which shows a white speck along the (001) zone axis, indicating the sample's pseudo-cubic crystalline structure.

To study the phase composition and microstructure of $\text{Ge}_{0.9-x}\text{Sb}_{0.1}\text{P}_x\text{Te}$ samples, we used FESEM and EDS analysis, as shown in Fig. 2(a–d). The cross-sectional SEM picture of the fractal GSPT-2 compound in Fig. 2(a) demonstrates its high-density tight packing character. As shown in Fig. 2(b), the herringbone structure was investigated in the GSPT-2 sample as described in the paper [53]. The samples' herringbone structure is revealed, with domain lengths of 100–200 nm and stressed borders separating each domain [27]. Herringbone structure, grain boundaries, dislocations, and interfaces have all been shown to have a considerable impact on the lattice component of thermal conductivity [6,11,43]. Multiple phonon scattering occurs when the distance between them is close to the phonon's mean free route, resulting in lower thermal conductivity and a drop in κ_{lat} . Fig. 2(c) depicts the polished surface of the GSPT-2 pellet, as well as EDS element mapping (d). The element distribution in the GSPT-2 samples was uniform, with no precipitations or secondary phases, which supported the PXRD.

Fig. 3 displays the TEM pictures of the GSPT-2 sample as well as the high-resolution domain analysis. Fig. 3(a) shows a bright-field TEM picture of a herringbone-like structure in GeTe that reveals domain variations with bright and dark contrast [21,53]. Fig. 3(b) depicts the GSPT-2 selective area electron diffraction pattern with twin domain grain boundaries. The strained domains and domain borders are shown in Fig. 3(c); the doping of Sb/P at the Ge site has caused extra strain, which will be relieved at either end of the domain. Such barriers include a variety of stresses, including compressive, tensile, and disordered at atomic sites; Fig. 3(d) depicts the

strained boundaries of the GSPT-2 sample. The highly disordered and mass fluctuating Ge/Sb/P sites, strained domain borders, and mesoscale domains will all contribute to the system's extensive phonon scattering mechanism.

3.2. Electronic structure

Fig. 4 shows the computed density of states (DOS) and partial density of states (PDOS) of GeTe, $\text{Ge}_{0.9}\text{Sb}_{0.1}\text{Te}$, and $\text{Ge}_{0.9-x}\text{Sb}_{0.1}\text{P}_x\text{Te}$ for the cubic phase. To investigate orbital involvement in the band structure, we estimated the total DOS and the PDOS, as shown in Fig. 4(a). The conduction band (CB) minimum is dominated by Ge $4p^2$ orbitals, while Te $5p^4$ orbitals govern the valance band (VB) maximum. The computed DOS and PDOS of Sb-doped GeTe are shown in Fig. 4(b). When Sb dopants are introduced, the CB minimum is dominated by mixed orbitals of Ge $4p^2$ and Sb $5p^3$, but the VB maximum is dominated by Te $5p^4$ orbitals. $\text{Ge}_{0.9}\text{Sb}_{0.1}\text{Te}$ DFT simulations indicate a unique state close to the CB minimum, anchoring the Fermi level (E_F). This state is mainly induced by the hybridization of Sb $5p^3$ and Ge $4p^2$ orbitals. The computed DOS of P doped $\text{Ge}_{0.9-x}\text{Sb}_{0.1}\text{P}_x\text{Te}$ is shown in Fig. 4(c) and (d). As illustrated in Fig. 4(c and d), two doping concentrations, $\text{Ge}_{0.875}\text{P}_{0.025}\text{Sb}_{0.1}\text{Te}$ and $\text{Ge}_{0.85}\text{P}_{0.05}\text{Sb}_{0.1}\text{Te}$, are explored; distortion in the CB minimum suggests a rise in electrical conductivity and power factor, which is further observed in the TE electrical transport properties. The $3p^3$ orbital of the P atom, as well as the $4p^2$ and $5p^3$ orbitals of the Ge and Sb atoms contribute to $\text{Ge}_{0.875}\text{P}_{0.025}\text{Sb}_{0.1}\text{Te}$'s DOS. Domination of the $3p^3$ orbital of the P atom is detected when P doping is increased (2.5–5 %), as shown in Fig. 4(d). Strong hybridization between the P, Sb, and host atoms is detected around the Fermi level (–1 to 1 eV) in

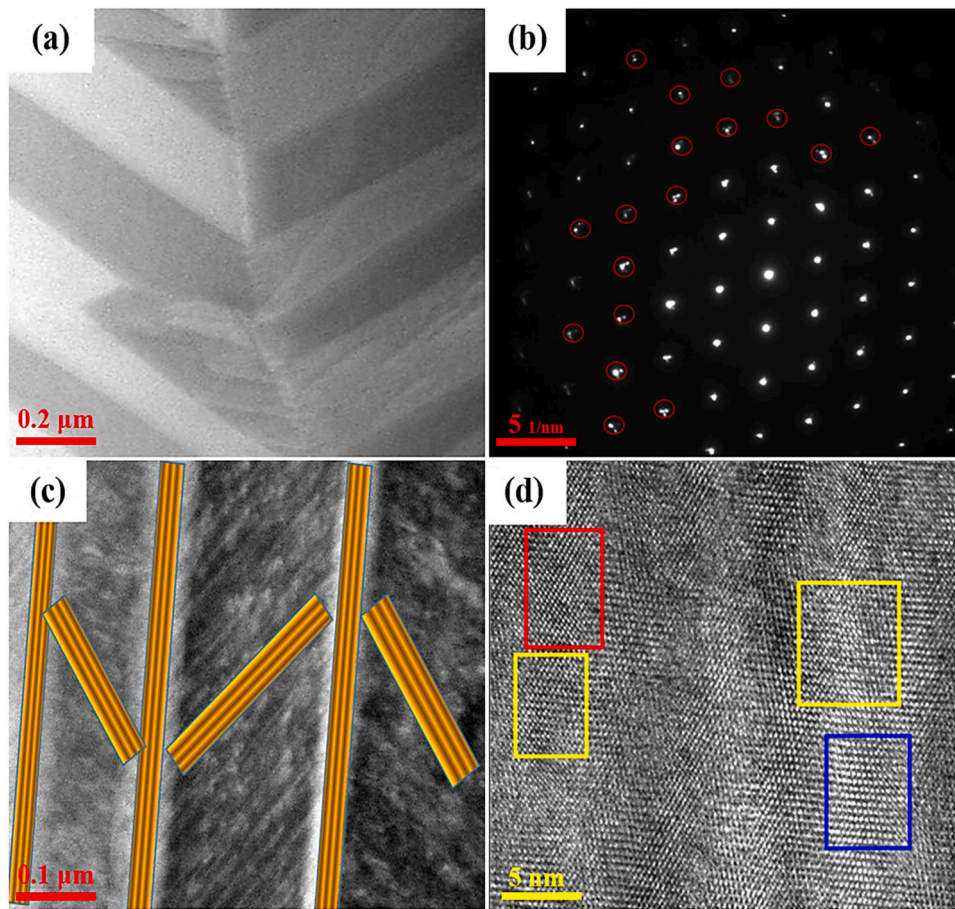


Fig. 3. High-resolution TEM images of GSPT-2 sample; (a) Herringbone structure; (b) Twin domains SAED pattern; (c) Highly strained grain boundaries; and (d) HR-TEM images strained region [compressive (red box), tensile (blue box), and highly atomic disordered (yellow box)].

both instances, suggesting strong covalent interaction, beneficial for the TE high-performance. Fig. S2 depicts the calculated band structure to manifest the role of P doping in the cubic GeTe phase.

3.3. Thermoelectric transport properties

The temperature-dependent electrical transport parameters of the $\text{Ge}_{0.9-x}\text{Sb}_{0.1}\text{P}_x\text{Te}$ sample are shown in Fig. 5 and compared with the $\text{Ge}_{0.9}\text{Sb}_{0.1}\text{Te}$ [27]. As seen in Fig. 5(a), the electrical conductivity (σ) decreases with increasing temperature, indicating degenerate semiconductor behavior. The σ reduced for the composition of $x = 0.01$, comparable to $\text{Ge}_{0.9}\text{Sb}_{0.1}\text{Te}$, which resembles the system's reduced Ge vacancies for $P \sim 0.01$ at% doping. Further increasing the P content reduced carrier concentration up to 3 at%, simultaneously enhancing the cubic nature of the system comprehended in the mobility increment. The composition-dependent mobility (μ) and carrier concentration (n) are illustrated in Fig. 5(b); when the P (+3) content increased, the carrier concentration decreased up to $x = 0.03$ but afterward increased owing to the electron donor nature of the carrier ($n = n_e + n_h$). The increase in mobility might be attributed to the rise in cubic nature (2θ between 41 and 45°); optimization of carrier concentration and mobility has resulted in an increase in the electrical conductivity of the $\text{Ge}_{0.9-x}\text{Sb}_{0.1}\text{P}_x\text{Te}$ sample. Electrical conductivity is defined in semiconductor physics as $\sigma = ne\mu$, where n denotes charge carrier concentration, μ represents carrier mobility, and e indicates the material's electrical charge. At 323 K, the electrical conductivity increases from 620 S/cm to 1020 S/cm. The high carrier concentration is obtained by high-level doping to ensure that

electricity is transported smoothly, as well as the high carrier mobility needed by the electrical conductivity expression. Figs. 4(c and d) and S2 depict the Fermi level shifting inside the CB as the Sb/P (+3) dopant concentration increases. Finally, we get an optimal value for n and μ of the $\text{Ge}_{0.9-x}\text{Sb}_{0.1}\text{P}_x\text{Te}$ systems with the addition of P (Fig. 5(b)). The reported electrical conductivity data show an increase near 523 – 623 K, which may correspond to the phase change to high-temperature (β -GeTe) from low-temperature (α -GeTe) [11,36]. The transformation from rhombohedral to the cubic structure shrunk the lattice to convert into the cubic symmetric lattice (mobility higher). While the material passes through the phase change temperature, an excess carrier generation will happen due to the lattice shrink [54], which can be seen in the electrical conductivity improvement.

The temperature-dependent Seebeck coefficient is shown in Fig. 5(c), which reveals that the Seebeck coefficient rises with increasing temperature in all samples up to 3 at% owing to a drop in carrier concentration (n). For $x = 0.01$ – 0.03 , the understood impact of the carrier concentration is more significant than the improved mobility of the systems; nevertheless, for $x > 0.03$, the n increases, causing a minor drop in the Seebeck values of $x = 0.04$ – 0.05 . When evaluated at temperatures ranging from 323 to 773 K, all $\text{Ge}_{0.9-x}\text{Sb}_{0.1}\text{P}_x\text{Te}$ samples provide a positive result, indicating the p -type nature of the materials. The highest Seebeck coefficient for GSPT-1 measured at 773 K is ~ 260 $\mu\text{V}/\text{K}$, higher than the previously reported value for the same temperature [22,27]. A considerable decrease in the Seebeck coefficient for $P = 0.04$ and 0.05 throughout the temperature range reflects an increase in secondary charge

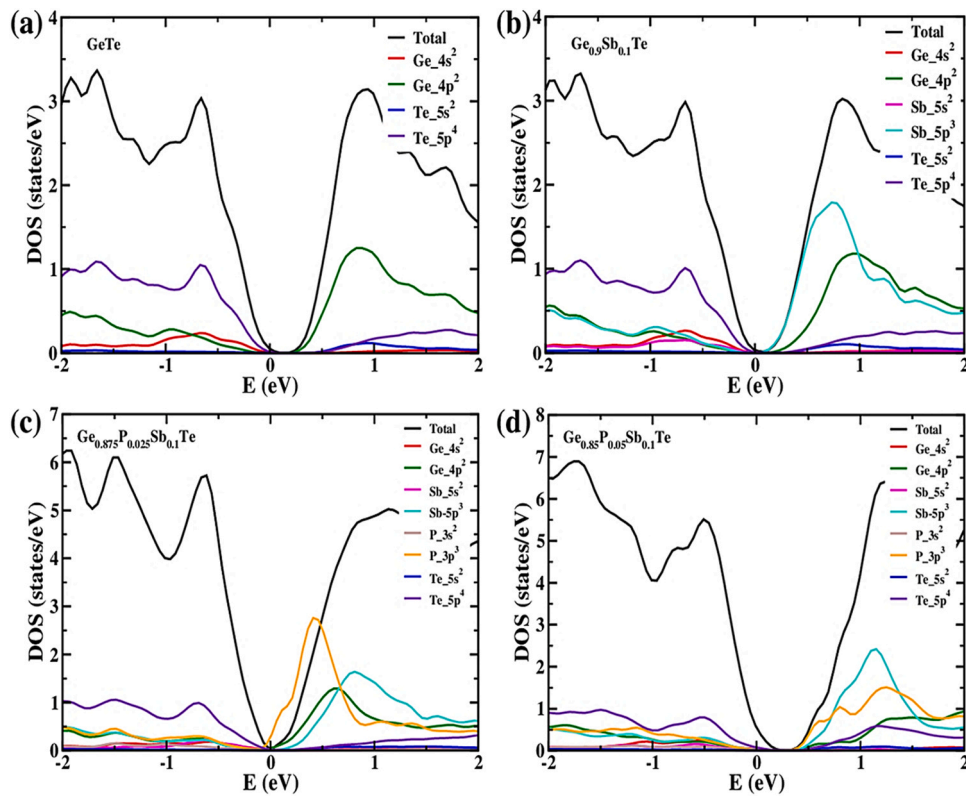


Fig. 4. Density of states (DOS) and partial DOS for the pristine and doped GeTe systems; (a) GeTe, (b) $\text{Ge}_{0.9}\text{Sb}_{0.1}\text{Te}$, (c) $\text{Ge}_{0.875}\text{P}_{0.025}\text{Sb}_{0.1}\text{Te}$, and (d) $\text{Ge}_{0.85}\text{Sb}_{0.1}\text{P}_{0.05}\text{Te}$. For clear visualization, the total DOS of all systems is reduced by a factor of 10. In all cases, VBM is pinned at 0.

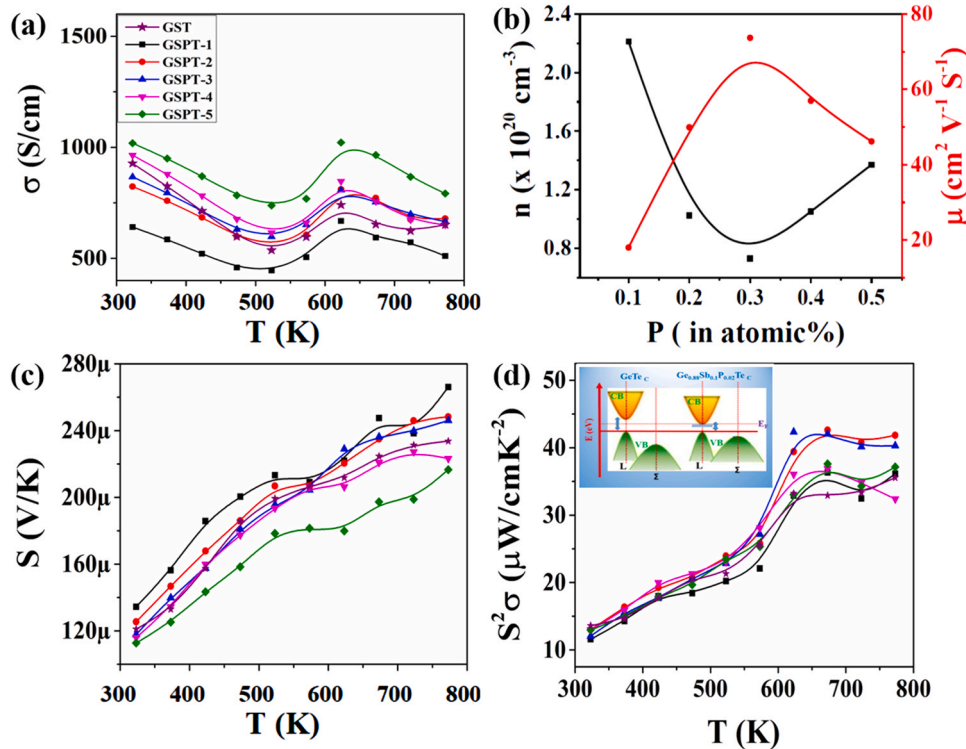


Fig. 5. Temperature-dependent electrical transport properties of P co-doped $\text{Ge}_{0.9}\text{Sb}_{0.1}\text{Te}$; (a) Electrical conductivity; (b) Compositional-dependent carrier concentration and mobility; (c) Seebeck coefficient; and (d) Power factor.

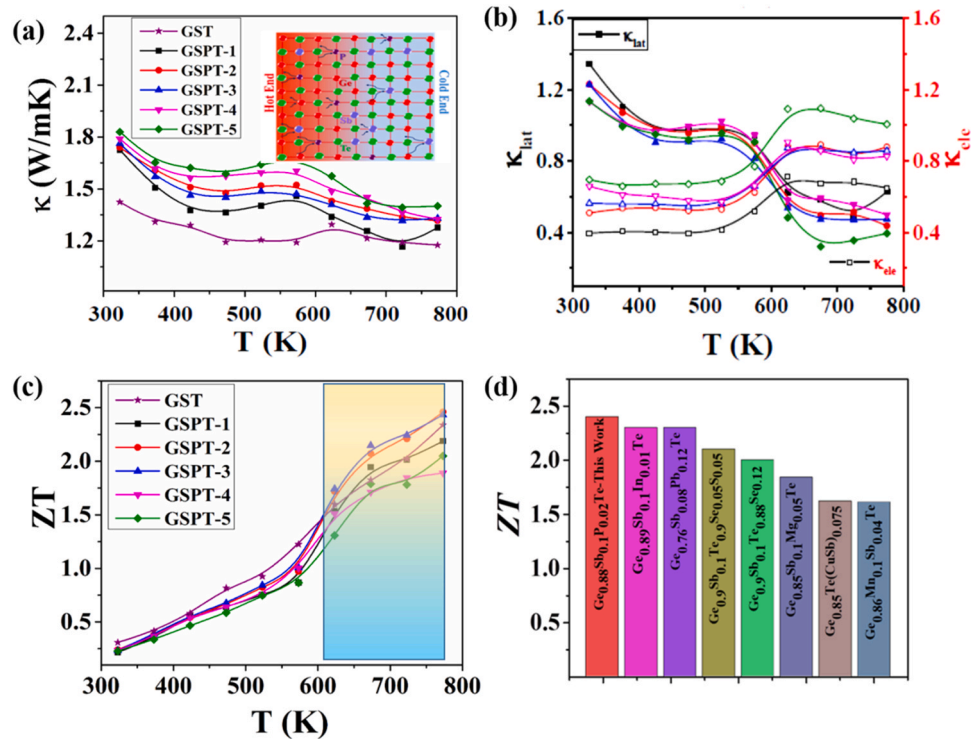


Fig. 6. Temperature-dependent thermal conductivity and thermoelectric performance of P co-doped $\text{Ge}_{0.9}\text{Sb}_{0.1}\text{Te}$: (a) Total thermal conductivity; (b) Electronic and lattice thermal conductivity; (c) ZT , and (d) State of the art.

carriers (e) originating from the dopant, respectively, which can be interpreted from the Eq. (2):

$$S = \frac{\sigma_e S_e + \sigma_h S_h}{\sigma_e + \sigma_h} \quad (2)$$

Here, σ_e , σ_h , S_e , and S_h represent electrical conductivity and Seebeck coefficient contributions from electrons and holes [55]. A plot of PF over the temperature range 323–723 K is shown in Fig. 5(d). For GSPT-2 and GSPT-3 samples, the power factor ($S^2\sigma$) increases and saturates at ~ 40 – $42 \mu\text{W cm}^{-1}\text{K}^{-2}$ following the phase transition with an increase in temperature. The highest PF observed in the GSPT-2 sample at 673 K was $42 \mu\text{W cm}^{-1}\text{K}^{-2}$. The enhancement in the PF of $x = 0.02$ & 0.03 over the $\text{Ge}_{0.9}\text{Sb}_{0.1}\text{Te}$ is attributed to the enhanced electrical as well as uncompromised Seebeck coefficients.

Fig. 6(a) depicts the temperature-dependent thermal conductivity (κ) of $\text{Ge}_{0.9-x}\text{Sb}_{0.1}\text{P}_x\text{Te}$ at various temperatures. A systematic enhancement was observed for the $x = 0.01$ – 0.05 at% over the $\text{Ge}_{0.9}\text{Sb}_{0.1}\text{Te}$ due to its increased cubic nature, which eventually electronically contributes to more thermal conductivity. A slight increase in thermal conductivity at 573 K, reported in P doping samples, is similar to the phase change phenomena observed in the sample's electrical conductivity. The increase in the thermal conductivity may be related to the phase transition of the samples at that temperature. The microstructure of TE materials is changed as the temperature increases. In addition, the materials undergo phase transitions when the temperature rises [27]. The disruption of the whole phonon spectrum (atomic scale (inset), nanoscale (domains and borders), and mesoscale (grain boundaries) are responsible for the total thermal conductivity drop. For the GSPT-2 sample, the lowest value of κ observed is $\sim 1.35 \text{ W/m K}$ at 773 K. In order to examine further, we calculated the electronic thermal conductivity (κ_{ele}) and lattice thermal conductivity (κ_{lat}) of the $\text{Ge}_{0.9-x}\text{Sb}_{0.1}\text{P}_x\text{Te}$ samples, and the results are shown in Fig. 6(b). All around, moderately low values of κ were observed in all samples. These

significantly lowered values are due to two causes. The first is an optimized carrier contribution to heat transport, and the second is increased phonon scattering due to various scattering processes [14,27,56]. The lattice contribution has gradually decreased because of increased scattering effects of mass variations (Ge, Sb, P), strain in the lattice, domain boundaries, and micro domains. On the other hand, its electron doping has been credited with some electrical contributions.

The temperature-dependent thermoelectric performance (ZT) of $\text{Ge}_{0.9-x}\text{Sb}_{0.1}\text{P}_x\text{Te}$ samples is shown in Fig. 6(c). Compared to the pristine GeTe and GeTe compounds with Sb doped, ZT values are significantly enhanced with Sb doping and P co-doping. The sample GSPT-2 attained the highest ZT value of ~ 2.4 at 773 K, with an average ZT value over 2 from 623 to 773 K. The improved carrier contribution and decreased lattice thermal conductivity resulted in a higher ZT in $\text{Ge}_{0.9-x}\text{Sb}_{0.1}\text{P}_x\text{Te}$ samples. The $\text{Ge}_{0.88}\text{Sb}_{0.1}\text{P}_{0.02}\text{Te}$ sample with the state-of-the-art ZT of GeTe compounds with excellent thermoelectric performance is shown in Fig. 6(d) [30,32,33,36,38,40,41].

4. Conclusion

A deliberate emphasis on electron doping and systematic management of lattice strain minimizes the contribution of lattice thermal conductivity to overall thermal conductivity. The double aliovalent (Sb/P) doping and Ge vacancy control by a two-step post-melt-quenching approach is shown to be superior to prior studies of multiple co-doping trials, giving a mechanism for enhanced ZT . FE-SEM and HR-TEM studies were used to study herringbone microdomains with higher lattice strain. An optimized carrier concentration (n) enables a $\sim 42 \mu\text{W cm}^{-1}\text{K}^{-2}$ power factor enhancement, and a significantly reduced thermal conductivity of $\sim 1.35 \text{ W/mK}$ at 773 K is demonstrated to be responsible for the high thermoelectric performance, $ZT \sim 2.4$ for GeTe with 2–3 at% P co-doped in Ge site. In the operating temperature range, the highest ZT value for p -type

$\text{Ge}_{0.88}\text{Sb}_{0.1}\text{P}_{0.02}\text{Te}$ was obtained and the most significant state-of-the-art average ZT value of ~ 2 (623–773 K).

CRedit authorship contribution statement

KSB prepared samples, **KSB** and **SI** collected all scientific data, analyzed and wrote the manuscript, **MU** & **AZ** did all the theoretical DFT calculations, **KHC** and **RS** guidance, funding and correction of manuscript.

Data availability

No data was used for the research described in the article.

Declaration of Competing Interest

The authors declare that they have no known competing financial interests or personal relationships that could have appeared to influence the work reported in this paper.

Acknowledgements

The authors gratefully acknowledge the AS-SS-109-01 project funding for thermoelectric material for sustainable energy. RS gratefully welcomes financial assistance from Taiwan's Ministry of Science and Technology under project number MOST-108-2112-M-001-049-MY2 and Academia Sinica for the AS-iMATE-109-13 budget. Safdar Imam thanks the MOE Taiwan scholarship for financial assistance. The authors would like to thank the Taiwan Photon Source (TPS) at the National Synchrotron Radiation Research Center (NSRRC) for allowing them to investigate temperature-dependent synchrotron X-ray diffraction (XRD) data. We want to thank the National PARAM Supercomputing Facility at the Centre for Development of Advanced Computing in Pune for computational assistance.

Appendix A. Supporting information

Supplementary data associated with this article can be found in the online version at [doi:10.1016/j.jallcom.2022.166221](https://doi.org/10.1016/j.jallcom.2022.166221).

References

- [1] D. Kraemer, B. Poudel, H.P. Feng, J.C. Caylor, B. Yu, X. Yan, Y. Ma, X. Wang, D. Wang, A. Muto, High-performance flat-panel solar thermoelectric generators with high thermal concentration, *Nat. Mater.* 10 (2011) 532–538.
- [2] Y.S. Jung, D.H. Jeong, S.B. Kang, F. Kim, M.H. Jeong, K.S. Lee, J.S. Son, J.M. Baik, J.-S. Kim, K.J. Choi, Wearable solar thermoelectric generator driven by unprecedentedly high temperature difference, *Nano Energy* 40 (2017) 663–672.
- [3] T. Xing, Q. Song, P. Qiu, Q. Zhang, M. Gu, X. Xia, J. Liao, X. Shi, L. Chen, High efficiency GeTe-based materials and modules for thermoelectric power generation, *Energy Environ. Sci.* 14 (2021) 995–1003.
- [4] J. Cao, X.Y. Tan, N. Jia, J. Zheng, S.W. Chien, H.K. Ng, C.K.I. Tan, H. Liu, Q. Zhu, S. Wang, Designing good compatibility factor in segmented $\text{Bi}_{0.5}\text{Sb}_{1.5}\text{Te}_3$ -GeTe thermoelectrics for high power conversion efficiency, *Nano Energy* 96 (2022) 107147.
- [5] G.J. Snyder, E.S. Toberer, Complex thermoelectric materials, in: *Materials for sustainable energy: a collection of peer-reviewed research and review articles from Nature Publishing Group*, World Scientific, 2011, pp. 101–110.
- [6] K. Biswas, J. He, I.D. Blum, C.I. Wu, T.P. Hogan, D.N. Seidman, V.P. Dravid, M.G. Kanatzidis, High-performance bulk thermoelectrics with all-scale hierarchical architectures, *Nature* 489 (2012) 414–418.
- [7] Q. Zhang, Q. Song, X. Wang, J. Sun, Q. Zhu, K. Dahal, X. Lin, F. Cao, J. Zhou, S. Chen, Deep defect level engineering: a strategy of optimizing the carrier concentration for high thermoelectric performance, *Energy Environ. Sci.* 11 (2018) 933–940.
- [8] X. Zhou, Y. Yan, X. Lu, H. Zhu, X. Han, G. Chen, Z. Ren, Routes for high-performance thermoelectric materials, *Mater. Today* 21 (2018) 974–988.
- [9] J. Kennedy, P.P. Murmu, P. Kumar, G. Ramanath, Multifold enhancements in thermoelectric power factor in isovalent sulfur doped bismuth antimony telluride films, *Mat. Res. Bull.* 142 (2021) 111426.
- [10] P.P. Murmu, J. Kennedy, S. Suman, S.V. Chong, J. Leveueur, J. Storey, S. Rubanov, G. Ramanath, Multifold improvement of thermoelectric power factor by tuning bismuth and antimony in nanostructured n-type bismuth antimony telluride thin films, *Mater. Des.* 163 (2019) 107549.
- [11] X. Zhang, Z. Bu, S. Lin, Z. Chen, W. Li, Y. Pei, GeTe thermoelectrics, *Joule* 4 (2020) 986–1003.
- [12] S. Zhi, J. Li, L. Hu, J. Li, N. Li, H. Wu, F. Liu, C. Zhang, W. Ao, H. Xie, Medium entropy-enabled high performance cubic GeTe thermoelectrics, *Adv. Sci.* 8 (2021) 2100220.
- [13] D. Dangi, O. Hellman, S. Fahy, I. Savic, The origin of the lattice thermal conductivity enhancement at the ferroelectric phase transition in GeTe, *npj Comput. Mater.* 7 (2021) 1–8.
- [14] N. Jia, J. Cao, X.Y. Tan, J. Dong, H. Liu, C.K.I. Tan, J. Xu, Q. Yan, X.J. Loh, A. Suwardi, Thermoelectric materials and transport physics, *Mater. Today Phys.* 21 (2021) 100519.
- [15] S.Y. Back, J.H. Yun, H. Cho, S. Byeon, H. Jin, J.S. Rhyee, High thermoelectric performance by chemical potential tuning and lattice anharmonicity in $\text{GeTe}_{1-x}\text{Sb}_x$ compounds, *Inorg. Chem. Front.* 8 (2021) 1205–1214.
- [16] S. Perumal, S. Roychowdhury, K. Biswas, High performance thermoelectric materials and devices based on GeTe, *J. Mater. Chem. C* 4 (2016) 7520–7536.
- [17] Y.F. Tsai, P.C. Wei, L. Chang, K.K. Wang, C.C. Yang, Y.C. Lai, C.R. Hsing, C.M. Wei, J. He, G.J. Snyder, Compositional fluctuations locked by athermal transformation yielding high thermoelectric performance in GeTe, *Adv. Mater.* 33 (2021) 2005612.
- [18] R. Zhang, J. Pei, Z. Shan, W. Zhou, Y. Wu, Z. Han, Y.-H. Zhao, J.F. Li, Z.H. Ge, B.P. Zhang, Intrinsic vacancy suppression and band convergence to enhance thermoelectric performance of (Ge, Bi, Sb) Te crystals, *Chem. Eng. J.* 429 (2022) 132275.
- [19] D.Z. Wang, W.D. Liu, M. Li, L.C. Yin, H. Gao, Q. Sun, H. Wu, Y. Wang, X.L. Shi, X. Yang, Simultaneously achieving high ZT and mechanical hardness in highly alloyed GeTe with symmetric nanodomains, *Chem. Eng. J.* 441 (2022) 136131.
- [20] T. Chattopadhyay, J. Boucherle, Neutron diffraction study on the structural phase transition in GeTe, *J. Phys. C Solid State Phys.* 20 (1987) 1431.
- [21] M. Snykers, P. Delavignette, S. Amelinckx, The domain structure of GeTe as observed by electron microscopy, *Mater. Res. Bull.* 7 (1972) 831–839.
- [22] K.S. Bayikadi, R. Sankar, C.T. Wu, C. Xia, Y. Chen, L.C. Chen, K.H. Chen, F.C. Chou, Enhanced thermoelectric performance of GeTe through in situ microdomain and Ge-vacancy control, *J. Mater. Chem. A* 7 (2019) 15181–15189.
- [23] Y. Jin, D. Wang, Y. Qiu, L.D. Zhao, Boosting the thermoelectric performance of GeTe by manipulating the phase transition temperature via Sb doping, *J. Mater. Chem. C* 9 (2021) 6484–6490.
- [24] J. Li, X. Zhang, Z. Chen, S. Lin, W. Li, J. Shen, I.T. Witting, A. Faghaninia, Y. Chen, A. Jain, Low-symmetry rhombohedral GeTe thermoelectrics, *Joule* 2 (2018) 976–987.
- [25] M. Li, Q. Sun, S.D. Xu, M. Hong, W.Y. Lyu, J.X. Liu, Y. Wang, M. Dargusch, J. Zou, Z.G. Chen, Optimizing electronic quality factor toward high-performance $\text{Ge}_{1-x}\text{yTa}_x\text{Sb}_y\text{Te}$ thermoelectrics: the role of transition metal doping, *Adv. Mater.* 33 (2021) 2102575.
- [26] S. Duan, W. Xue, H. Yao, X. Wang, C. Wang, S. Li, Z. Zhang, L. Yin, X. Bao, L. Huang, Achieving high thermoelectric performance by NaSbTe_2 alloying in GeTe for simultaneous suppression of Ge vacancies and band tailoring, *Adv. Energy Mater.* 12 (2022) 2103385.
- [27] K.S. Bayikadi, C.T. Wu, L.C. Chen, K.H. Chen, F.C. Chou, R. Sankar, Synergistic optimization of thermoelectric performance of Sb doped GeTe with a strained domain and domain boundaries, *J. Mater. Chem. A* 8 (2020) 5332–5341.
- [28] C. Li, H. Song, Z. Dai, Z. Zhao, C. Liu, H. Yang, C. Cui, L. Miao, High thermoelectric performance achieved in Sb-doped GeTe by manipulating carrier concentration and nanoscale twin grains, *Materials* 15 (2022) 406.
- [29] L. Xie, Y. Chen, R. Liu, E. Song, T. Xing, T. Deng, Q. Song, J. Liu, R. Zheng, X. Gao, Stacking faults modulation for scattering optimization in GeTe-based thermoelectric materials, *Nano Energy* 68 (2020) 104347.
- [30] L. Yue, T. Fang, S. Zheng, W. Cui, Y. Wu, S. Chang, L. Wang, P. Bai, H. Zhao, Cu/Sb codoping for tuning carrier concentration and thermoelectric performance of GeTe-based alloys with ultralow lattice thermal conductivity, *ACS Appl. Energy Mater.* 2 (2019) 2596–2603.
- [31] H. Kim, C.O. Park, H. Jeong, S.K. Kihoi, S. Yi, H.S. Kim, K.H. Lee, H.S. Lee, Generation of multi-dimensional defect structures for synergetic engineering of hole and phonon transport: enhanced thermoelectric performance in Sb and Cu co-doped GeTe, *Inorg. Chem. Front.* 8 (2021) 2782–2787.
- [32] J. Li, X. Zhang, S. Lin, Z. Chen, Y. Pei, Realizing the high thermoelectric performance of GeTe by Sb-doping and Se-alloying, *Chem. Mater.* 29 (2017) 605–611.
- [33] T. Xing, Q. Song, P. Qiu, Q. Zhang, X. Xia, J. Liao, R. Liu, H. Huang, J. Yang, S. Bai, Superior performance and high service stability for GeTe-based thermoelectric compounds, *Natl. Sci. Rev.* 6 (2019) 944–954.
- [34] T. Xing, C. Zhu, Q. Song, H. Huang, J. Xiao, D. Ren, M. Shi, P. Qiu, X. Shi, F. Xu, Ultralow lattice thermal conductivity and superhigh thermoelectric figure-of-merit in (Mg, Bi) Co-doped GeTe, *Adv. Mater.* 33 (2021) 2008773.
- [35] E. Nshimiyimana, S. Hao, X. Su, C. Zhang, W. Liu, Y. Yan, C. Uher, C. Wolverton, M.G. Kanatzidis, X. Tang, Discordant nature of Cd in GeTe enhances phonon scattering and improves band convergence for high thermoelectric performance, *J. Mater. Chem. A* 8 (2020) 1193–1204.
- [36] M. Hong, Z.G. Chen, L. Yang, Y.C. Zou, M.S. Dargusch, H. Wang, J. Zou, Realizing zT of 2.3 in $\text{Ge}_{1-x}\text{ySb}_x\text{In}_y\text{Te}$ via reducing the phase-transition temperature and introducing resonant energy doping, *Adv. Mater.* 30 (2018) 1705942.
- [37] S. Imam, K.S. Bayikadi, M. Ubaid, V. Ranganayakulu, S. Devi, B.S. Pujari, Y.Y. Chen, L.-C. Chen, K.H. Chen, F.L. Lin, Achieving synergistic performance through highly compacted microcrystalline rods induced in Mo doped GeTe based compounds, *Mater. Today Phys.* 22 (2022) 100571.

- [38] Z. Zheng, X. Su, R. Deng, C. Stoumpos, H. Xie, W. Liu, Y. Yan, S. Hao, C. Uher, C. Wolverton, Rhombohedral to cubic conversion of GeTe via MnTe alloying leads to ultralow thermal conductivity, electronic band convergence, and high thermoelectric performance, *J. Am. Chem. Soc.* 140 (2018) 2673–2686.
- [39] A. Kumar, P. Bhumla, T. Parashchuk, S. Baran, S. Bhattacharya, K.T. Wojciechowski, Engineering electronic structure and lattice dynamics to achieve enhanced thermoelectric performance of Mn–Sb Co-doped GeTe, *Chem. Mater.* 33 (2021) 3611–3620.
- [40] M. Samanta, K. Biswas, Low thermal conductivity and high thermoelectric performance in $(\text{GeTe})_{1-2x}(\text{GeSe})_x(\text{GeS})_x$: competition between solid solution and phase separation, *J. Am. Chem. Soc.* 139 (2017) 9382–9391.
- [41] X. Zhang, J. Li, X. Wang, Z. Chen, J. Mao, Y. Chen, Y. Pei, Vacancy manipulation for thermoelectric enhancements in GeTe alloys, *J. Am. Chem. Soc.* 140 (2018) 15883–15888.
- [42] W. Gao, Z. Liu, W. Zhang, N. Sato, Q. Guo, T. Mori, Improved thermoelectric performance of GeTe via efficient yttrium doping, *Appl. Phys. Lett.* 118 (2021) 033901.
- [43] N. Jia, J. Cao, X.Y. Tan, J. Zheng, S.W. Chien, L. Yang, K. Chen, H.K. Ng, S.S.F. Duran, H. Liu, Suppressing Ge-vacancies to achieve high single-leg efficiency in GeTe with an ultra-high room temperature power factor, *J. Mater. Chem. A* 9 (2021) 23335–23344.
- [44] C. Zhu, F. Luo, J. Wang, S. Zhang, J. Wang, H. Liu, Z. Sun, Realizing high thermoelectric performance in GeTe by defect engineering on cation sites, *J. Mater. Chem. C* (2022).
- [45] W.Y. Lyu, W.D. Liu, M. Li, M. Hong, K. Guo, J. Luo, J. Xing, Q. Sun, S. Xu, J. Zou, The effect of rare earth element doping on thermoelectric properties of GeTe, *Chem. Eng. J.* (2022) 137278.
- [46] J.R. Gandhi, R. Nehru, S.M. Chen, R. Sankar, K.S. Bayikadi, P. Sureshkumar, K.H. Chen, L.C. Chen, Influence of GeP precipitates on the thermoelectric properties of p-type GeTe and $\text{Ge}_{0.9-x}\text{P}_x\text{Sb}_{0.1}\text{Te}$ compounds, *Cryst. Eng. Comm.* 20 (2018) 6449–6457.
- [47] P. Giannozzi, S. Baroni, N. Bonini, M. Calandra, R. Car, C. Cavazzoni, D. Ceresoli, G.L. Chiarotti, M. Cococcioni, I. Dabo, QUANTUM ESPRESSO: a modular and open-source software project for quantum simulations of materials, *J. Phys. Condens. Matter* 21 (2009) 395502.
- [48] D. Vanderbilt, Soft self-consistent pseudopotentials in a generalized eigenvalue formalism, *Phys. Rev. B* 41 (1990) 7892.
- [49] J.P. Perdew, K. Burke, M. Ernzerhof, Generalized gradient approximation made simple, *Phys. Rev. Lett.* 77 (1996) 3865.
- [50] H.J. Monkhorst, J.D. Pack, Special points for Brillouin-zone integrations, *Phys. Rev. B* 13 (1976) 5188.
- [51] S. Perumal, S. Roychowdhury, D.S. Negi, R. Datta, K. Biswas, High thermoelectric performance and enhanced mechanical stability of p-type $\text{Ge}_{1-x}\text{Sb}_x\text{Te}$, *Chem. Mater.* 27 (2015) 7171–7178.
- [52] M.N. Schneider, X. Biquard, C. Stiewe, T. Schröder, P. Urban, O. Oeckler, From metastable to stable modifications—in situ Laue diffraction investigation of diffusion processes during the phase transitions of $(\text{GeTe})_n\text{Sb}_2\text{Te}_3$ ($6 < n < 15$) crystals, *Chem. Commun.* 48 (2012) 2192–2194.
- [53] H.S. Lee, B.S. Kim, C.W. Cho, M.W. Oh, B.K. Min, S.D. Park, H.W. Lee, Herringbone structure in GeTe-based thermoelectric materials, *Acta Mater.* 91 (2015) 83–90.
- [54] M. Sist, H. Kasai, E.M. Hedegaard, B.B. Iversen, Role of vacancies in the high-temperature pseudodisplacive phase transition in GeTe, *Phys. Rev. B* 97 (2018) 094116.
- [55] C. Kittel, *P. McEuen, Introduction to Solid State Physics*, John Wiley & Sons, 2018.
- [56] Y. Wu, Z. Chen, P. Nan, F. Xiong, S. Lin, X. Zhang, Y. Chen, L. Chen, B. Ge, Y. Pei, Lattice strain advances thermoelectrics, *Joule* 3 (2019) 1276–1288.